Journal of Computational Physics: X 8 (2020) 100071

Contents lists available at ScienceDirect

Journal of Computational Physics: X

www.elsevier.com/locate/jcpx

A mixed Eulerian-Lagrangian High-Order Spectral method for the propagation of ocean surface waves over a flat bottom

Sébastien Fouques *, Csaba Pákozdi

Department Ships and Ocean Structures, SINTEF Ocean, Trondheim, Norway

ARTICLE INFO

Article history:
Received 16 October 2019
Received in revised form 26 July 2020
Accepted 13 August 2020
Available online 19 August 2020

Keywords:
Sea surface waves
Spectral method
Lagrangian flow description

ABSTRACT

We introduce a numerical method to describe the propagation of two-dimensional nonlinear water waves over a flat bottom. The free surface is described in terms of a Lagrangian representation, i.e. by following the position and the velocity potential of a set of surface particles. The method consists in a mixed Eulerian-Lagrangian modification of the classical High-Order Spectral (HOS) method. At each time step, the Eulerian velocity potential inside the domain and the velocity of the surface particles are estimated by using a spectral decomposition along with a perturbation expansion at an arbitrary order M. The Lagrangian description of the surface makes it possible to use lower approximation orders and fewer Fourier modes to capture steep nonlinear waves, which also improves the numerical stability of the method. Its accuracy is established for steep regular waves by comparing simulations to existing Lagrangian and Eulerian solutions, as well as to traditional HOS-simulations. For irregular bichromatic waves, we show with an example that the obtained solution converges with respect to the Lagrangian conservation equations as the order M increases. Finally, the ability of the proposed method to compute the velocity field in steep irregular waves is demonstrated.

© 2020 The Author(s). Published by Elsevier Inc. This is an open access article under the CC BY license (http://creativecommons.org/licenses/by/4.0/).

1. Introduction

Many ocean engineering applications require the accurate modelling of random steep waves, sometimes up to the onset of breaking, as well as their probability of occurrence in a given sea state [1,2]. Owing to the nonlinear characteristics of the equations that govern the propagation of water waves, approximations have to be made in numerical models to achieve a targeted accuracy at an acceptable computational cost. The variety of applications has contributed to the development of numerous models, from linear wave theory, which remains valid for low steepness waves, to more complex models able to capture wave overturning [3]. However, performing random wave simulations that are able to efficiently capture both the physics and the probability of occurrence of extreme steep wave events has remained a challenge.

Recently, the High-Order Spectral (HOS) method introduced by [4] and [5] has been widely used for this purpose, and it has also been applied to enhance wave generation in experimental facilities [6,7]. A clear advantage of the HOS-method is that it can describe the propagation of nonlinear irregular waves over a flat bottom, up to a selected approximation order, and in either two or three dimensions. Thus, it is able to capture the modulational instability [8,9] responsible for the occurrence of extreme waves in deep water, and unlike the nonlinear Schrödinger equation [10], without any assumption regarding the spectral bandwidth [11]. Moreover, by using simple boundary conditions, the Laplace equation is integrated

* Corresponding author.
E-mail addresses: Sebastien.Fouques@sintef.no (S. Fouques), Csaba.Pakozdi@sintef.no (C. Pákozdi).

https://doi.org/10.1016/j.jcpx.2020.100071
2590-0552/© 2020 The Author(s). Published by Elsevier Inc. This is an open access article under the CC BY license (http://creativecommons.org/licenses/by/4.0/).

analytically, so that the velocity potential is written as a sum of spatial mode functions at each time step. Consequently, the HOS-method is relatively computationally efficient, since only surface equations have to be time-integrated. Still, it is based on a perturbation expansion, in which the wave steepness is assumed to be small, along with an Eulerian description of the free surface. The development of nonlinear steep waves is then characterized by an increase of high-frequency harmonics in the surface elevation spectrum, which results in instabilities in the numerical scheme [4]. Hence, in the absence of wave breaking treatment as proposed by e.g. [12,13], the applicability of the HOS-method is limited to sea states with moderate steepness [14]. Stability can be improved by reducing the number of Fourier modes, which results in rounded-shaped wave crests. Owing to its relative accuracy and efficiency, it can however be used to initialize more sophistical models based on e.g. CFD with the nonlinear surface elevation and the velocity field before the onset of breaking. The latter models are then used to propagate the wave further, and to compute the flow velocity during the breaking event [15,16] as well as possible wave-structure interactions. Special care has to be taken when deriving velocity fields in steep waves with the HOS-method, since convergence issues can be encountered in the vicinity of the crests [17,18].

The HOS-method relies on a traditional Eulerian formulation of the flow, which consists in expressing the surface elevation and the water velocity as functions of earth-fixed space coordinates x, y and z. The main advantage of this formulation is that, under the additional assumption that the flow is incompressible and irrotational, the whole velocity field can be derived from a single scalar function, namely the velocity potential, which satisfies the well-known linear Laplace equation. However, the boundary conditions to be fulfilled at the unknown free surface are nonlinear. Another approach to wave modelling consists in using a Lagrangian flow formulation, i.e. by following individual fluid particles, whose positions vary in time. Its main advantage is a more flexible parametric description of the free surface, which is especially beneficial to steep waves [19]. The kinematic and dynamic boundary conditions, expressed at the known free surface are linear and quadratic, respectively. However, the mass conservation written in terms of Lagrangian coordinates is nonlinear [20, pp. 12-14], which suppresses the mathematical convenience of the Laplace equation. The depth-dependent horizontal drift of the particles in waves is also an issue with respect to the steadiness of the solutions [21,22]. In spite of these complications, Lagrangian wave models have interesting properties. First of all, there exists an exact periodic wave solution, namely the Gerstner wave, that fulfils the mass and momentum conservation equations, as well the surface and bottom boundary conditions [23,24]. When the amplitude reaches its limiting value, the wave profile is an upside-down cycloid with infinite slope at the crest. Although this solution is rotational at the second order, which makes it of less applicability in practice for waves initiated from rest, it is close to the first- and second-order solutions originally proposed by [25] for two-dimensional irregular waves. A general feature of these Lagrangian solutions obtained from a perturbation expansion is that some nonlinear Eulerian features appear at lower orders. For example, the linear solution for irregular waves shows sharp crests and broad troughs [25], as well as a modulation of the wave height and the wavelength of short waves riding on the top of longer ones [26]. Second-order horizontal displacement waves are also responsible for the asymmetric steepening of wave fronts as they propagate through large wave groups [27]. For short-crested waves [28], horseshoe patterns are observed already at the second order as the result of a non-homogeneous drift current. Finally, [22] derived a seventh-order Lagrangian solution for steady regular waves in deep water, and noted that faster convergence is achieved with a Lagrangian representation, compared to usual Eulerian Stokes-like expansions.

In this paper, we propose a modification of the HOS method, in which the free surface is described with a Lagrangian representation. The method also makes use of the powerful properties of potential theory in its Eulerian form, and thus is referred to as mixed Eulerian-Lagrangian HOS (MELHOS). The basic idea of the MELHOS-method is to trade the two nonlinear functions used in the original HOS scheme, namely the surface elevation and the velocity potential at the surface, for three less nonlinear functions, the horizontal and vertical positions of surface particles, as well as the velocity potential obtained when following these surface particles. By doing so, fewer super-harmonics and lower approximation orders are needed, which in turn improves the accuracy and the stability of the numerical scheme for the simulation of steep waves. The paper briefly recalls some fundamental properties of the Lagrangian wave solutions, before describing the MELHOS method and its numerical implementation in Section 2. Verification, convergence tests and comparisons with the standard HOS method are then presented in Section 3 for regular and irregular waves. The ability of the MELHOS method to derive the velocity field in steep irregular waves is discussed in Section 4. Possible applications, limitations and extensions are finally discussed in Section 5.

2. Description of the model

2.1. Eulerian and Lagrangian flow descriptions

We consider the propagation of two-dimensional water waves in constant depth h. It is assumed that water is inviscid and incompressible, and the flow is irrotational. A cartesian coordinate system (x, y, z) is used with z positive upwards. The free surface is located at $z = 0$ in still water. In addition, we assume that the fluid is contained inside a rectangular domain with horizontal dimension L along x, and periodic boundary conditions at $x = 0$ and $x = L$. Finally, the statistical properties of the flow, such as the mean value and the variance of the flow velocity, are assumed to be horizontally homogeneous. The velocity field at any time t can then be written as $\mathbf{U}(x, z, t) = \nabla\phi_E$, where $\phi_E(x, z, t)$ is the usual Eulerian velocity potential, and where ∇ is the nabla operator with respect to x and z.

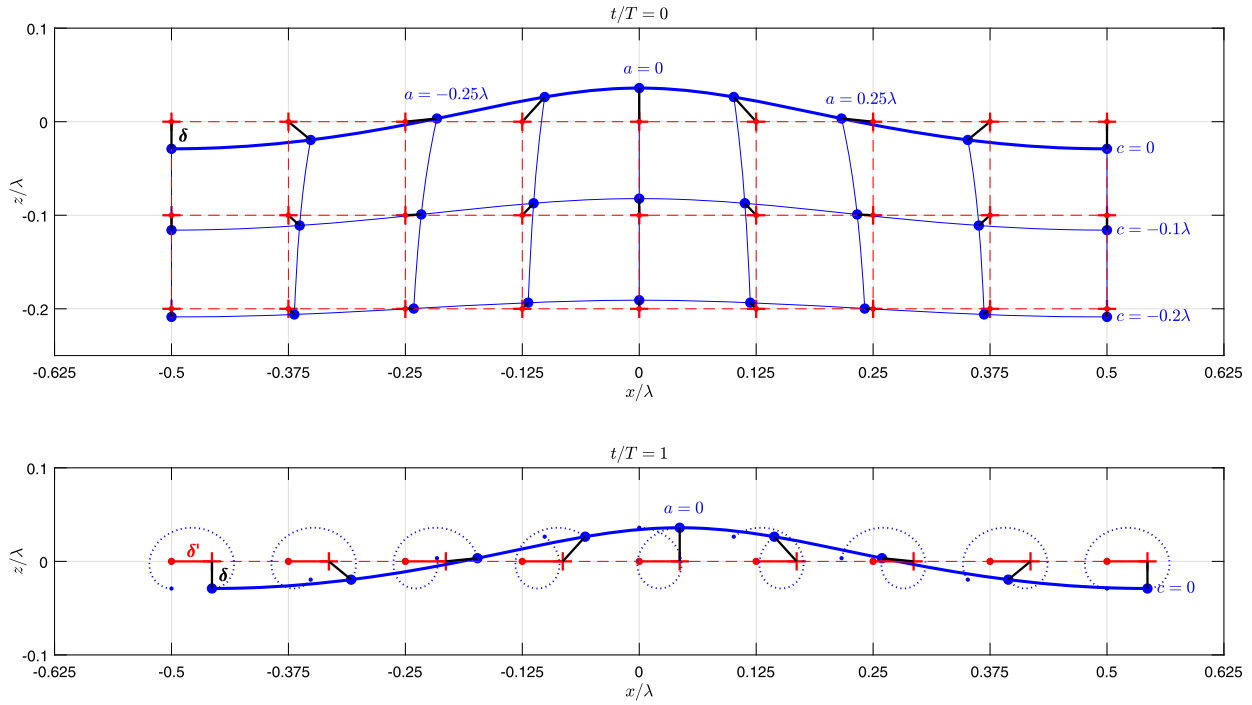

Fig. 1. Lagrangian representation of a regular surface wave with period T and wavelength λ at $t = 0$ (top) and $t = T$ (bottom, surface particles only). Blue circles: position of the particles with respect to their instantaneous orbit centers (red crosses). Blue dotted line: particle trajectory between $t = 0$ and $t = T$. Black segments: oscillatory part δ of the particles' displacement. Red segments: horizontal drift δ'. Red dots: original rest position at $(x, z) = (a, c)$.

In the Lagrangian specification, the water motion is described through a collection of fluid particles, labeled by continuous Lagrangian coordinates $\mathbf{X_0} = (a, c)^T$ that we choose equal to their (x, z)-positions in the absence of waves and at $t = 0$. Owing to the kinematic boundary conditions, bottom particles are then characterized by $c = -h$, and those at the surface by $c = 0$. We write the position $\mathbf{X} = (x_L, z_L)^T$ of the particles at any time t as

$$\mathbf{X}(a, c, t) = \mathbf{X_0} + \boldsymbol{\delta}(a, c, t) + \boldsymbol{\delta'}(c, t). \tag{1}$$

Here, the term $\boldsymbol{\delta} = (\delta_x, \delta_z)^T$ is bounded and represents the oscillatory motion of the particles. It consists of a sum of harmonic functions, as in the fourth-order regular wave solution proposed by [29] and given in Appendix A. Further, $\boldsymbol{\delta'} = (\delta'_x, 0)^T$ is a horizontal drift term, equal to zero at $t = 0$. The fact that $\boldsymbol{\delta'}$ does not depend on a is the result of the horizontal homogeneity assumption and is discussed further in Section 3.2. An illustration is provided for a regular wave in Fig. 1. Here, the positions of the particles are obtained from the fourth-order described in Appendix A, with $\varepsilon = 0.2$.

2.2. Lagrangian governing equations

The momentum and mass conservation equations written in Lagrangian coordinates read [20, pp. 12-14]

$$\mathbf{J}\ddot{\mathbf{X}} + \boldsymbol{\nabla}_{\boldsymbol{L}}\,(g z_L + p_L/\rho) = \mathbf{0} \tag{2}$$

$$\det(\mathbf{J}) = 1, \tag{3}$$

respectively, where $\boldsymbol{\nabla}_{\boldsymbol{L}}$ is the nabla operator with respect to the Lagrangian coordinates a and c, and with the Jacobian matrix

$$\mathbf{J} = \begin{bmatrix} \dfrac{\partial x_L}{\partial a} & \dfrac{\partial z_L}{\partial a} \\ \dfrac{\partial x_L}{\partial c} & \dfrac{\partial z_L}{\partial c} \end{bmatrix}. \tag{4}$$

Further, dot superscripts represent partial derivatives with respect to time, $p_L(a, c, t)$ is the water pressure at the position of the particles, g the acceleration due to gravity, and ρ the constant water density. The kinematic and dynamic free surface conditions read $c = 0$ at the surface and $p_L(a, c = 0, t) = 0$, respectively. As mentioned by e.g. [30] and [29], for an irrotational flow, the momentum conservation implies that

$$\nabla_{\boldsymbol{L}} \times (\mathbf{J}\dot{\mathbf{X}}) = \mathbf{0}, \tag{5}$$

which corresponds to the zero-vorticity condition $\nabla \times \mathbf{U} = \mathbf{0}$ in Lagrangian coordinates. It is noteworthy to mention that, unlike their Eulerian counterparts, the Lagrangian conservation of mass and momentum, as well the zero-vorticity condition, are nonlinear. However, the Lagrangian kinematic boundary condition is linear and explicitly written at $c = 0$, whereas the Eulerian equivalent

$$\dot{\eta} = \frac{\partial \phi_E}{\partial z} - \frac{\partial \phi_E}{\partial x}\frac{\partial \eta}{\partial x} \qquad \text{at} \qquad z = \eta(x,t), \tag{6}$$

is nonlinear and written on the unknown free surface.

2.3. Discussion of the Lagrangian steady wave solution

For the sake of clarity, we briefly repeat and discuss some fundamental characteristics of the Lagrangian wave models obtained by solving the Lagrangian equations presented in Section 2.2. The solution for a steady regular wave derived by [29] is given in Appendix A up to the fourth order for deep water, and it serves as the basis for the discussion below. Additional features for irregular long-crested and short-crested waves can be found for example in [25] and [28].

With the Lagrangian description, the surface elevation is given as a parametric representation that consists of two progressing waves, namely the horizontal and vertical particle displacements δ_x and δ_z. A priori, this allows more flexibility than the corresponding Eulerian representation $\eta(x)$. Horizontal δ_x-waves tend to cluster particles near the wave crests, where higher surface curvature requires more accurate space resolution [19]. In the regular wave solution provided in Appendix A, this advantage is reflected in fewer harmonics compared to its Eulerian counterpart [31]. For example, the second harmonics with phase 2Ψ appears only from the fourth-order solution in δ_x and δ_z, and not from the second-order one as in $\eta(x)$ [31]. This characteristic is also seen in the second-order solution for irregular waves [25], which do not contain any sum-frequency terms. In other words, high-frequency Eulerian bound waves are captured by the modulation of two less nonlinear processes instead of a single nonlinear one.

The Lagrangian representation is also a benefit for HOS-based methods, since the latter become unstable for highly nonlinear steep wave events [14]. In the two-dimensional HOS method proposed by [4] and [5], the wave propagation is described in terms of two functions: the Eulerian free surface elevation $\eta(x,t)$ and the velocity potential at the free surface $\phi_\Sigma(x,t) = \phi_E(x, z = \eta(x,t), t)$. For a regular wave in deep water with wave number k and amplitude ε_E/k, we have [31]

$$k\eta(x,t) = \left[\varepsilon_E - \frac{3}{8}\varepsilon_E^3\right]\cos\Psi_E + \frac{\varepsilon_E^2}{2}\cos(2\Psi_E) + \frac{3}{8}\varepsilon_E^3\cos(3\Psi_E) + O\left(\varepsilon_E^4\right) \tag{7}$$

$$\frac{k^2}{\sigma_0}\phi_\Sigma(x,t) = \left[\varepsilon_E - \frac{5}{8}\varepsilon_E^3\right]\sin\Psi_E + \frac{\varepsilon_E^2}{2}\sin(2\Psi_E) + \frac{3}{8}\varepsilon_E^3\sin(3\Psi_E) + O\left(\varepsilon_E^4\right), \tag{8}$$

with $\Psi_E = kx - \sigma_E t$, $\sigma_E = \sigma_0(1 + \varepsilon_E^2/2) + O\left(\varepsilon_E^4\right)$ and $\sigma_0^2 = kg$. With the Lagrangian description, three functions are needed, namely the position $\mathbf{X_S} = (x_S, z_S)^T$ of the surface particles, with $\mathbf{X_S}(a,t) = \mathbf{X}(a, c = 0, t)$, and the velocity potential $\phi_S(a,t) = \phi_E(x_S, z_S, t)$ at the position of the particles. For the same regular wave as above, these three functions can be written as [29] (see also Appendix A):

$$kx_s(a,t) = ka - \left[\varepsilon + \frac{3}{2}\varepsilon^3\right]\sin\Psi + \varepsilon^2\sigma_0 t + O\left(\varepsilon^4\right) \tag{9}$$

$$kz_s(a,t) = \frac{\varepsilon^2}{2} + \left[\varepsilon + \frac{1}{2}\varepsilon^3\right]\cos\Psi + O\left(\varepsilon^4\right) \tag{10}$$

$$\frac{k^2}{\sigma_0}\phi_S(a,t) = \varepsilon\sin\Psi + O\left(\varepsilon^4\right), \tag{11}$$

with $\Psi = ka - \sigma t$ and $\sigma = \sigma_0(1 - \varepsilon^2/2) + O\left(\varepsilon^4\right)$. Note that the Eulerian and Lagrangian wave amplitudes ε_E/k and ε/k, respectively, are slightly different, as will be shown in Section 3.1. By comparing (7)-(8) with (9)-(11), it appears that the Lagrangian description of the free surface is more linear than its Eulerian counterpart. Unlike η and ϕ_Σ, the third-order expressions of x_S, z_S and ϕ_S do not contain additional harmonics with phases 2Ψ and 3Ψ. Moreover, the velocity potential ϕ_S obtained when following surface particles do not contain any second- nor third-order terms. Thus, it remains linear within a fourth-order approximation.

A drawback of the Lagrangian description is its complexity, caused by the depth-dependent Stokes drift [25] in δ_x', combined with the fact the phase Ψ depends on the particle label a and not on the horizontal space coordinate x. This results in a depth-dependent phase velocity σ/k [32]. Moreover, the mass conservation (3) and zero-vorticity condition (5) are nonlinear. Consequently, in Mth-order solutions, these equations include secular terms of order $(M+1)$, which make them diverge as time increases [22]. In the MELHOS method presented in this paper, only surface particles are considered. Therefore, such issues related to the Lagrangian flow description below the free surface are not relevant, as will be shown

in Section 3.2. Nevertheless, typical Lagrangian features related to the drift of surface particles, as well as to the non-zero mean value of their vertical coordinate z_S, have to be treated carefully.

2.4. Mixed Eulerian-Lagrangian HOS scheme

The Lagrangian free surface boundary conditions can be expressed as [19]

$$\dot{\mathbf{X}}_\mathbf{S} = \nabla\phi_E(x_S, z_S, t) \tag{12}$$

$$\dot{\phi}_S = \frac{1}{2}\nabla\phi_E(x_S, z_S, t)^2 - g z_S. \tag{13}$$

Here, $\mathbf{X_S} = (x_S, z_S)^T$ and ϕ_S are functions of the Lagrangian coordinate a, so that the time derivatives in the left-hand side are simple partial derivatives. To use (12) and (13) as evolution equations to propagate the surface elevation, the velocity of the surface particles $\nabla\phi_E(x_S, z_S, t)$ has to be derived from the position $\mathbf{X_S}$ and the potential ϕ_S of the surface particles. In its Eulerian form, the mass conservation is expressed as the simple but powerful Laplace equation $\nabla^2\phi_E = 0$. By invoking the boundary conditions on the flat bottom at $z = -h$, and on the vertical walls at $x = 0$ and $x = L$, ϕ_E can be integrated to [4]

$$\phi_E(x, z, t) = \sum_p A_p(t) \exp\left(\mathrm{i}k_p x\right) \frac{\cosh\left(k_p[z+h]\right)}{\cosh\left(k_p h\right)}, \tag{14}$$

with $k_p = 2\pi p/L$ and where p is a positive integer. The modal amplitudes $A_p(t)$ are easily obtained by a Fourier transform of $\phi_E(x, 0, t)$ with respect to x. Consequently, the calculation of the entire flow is reduced to the determination of ϕ_E at $z = 0$. To derive the latter quantity from the Lagrangian functions $\boldsymbol{X_S}$ and ϕ_S, we first write a Taylor expansion of $\phi_E(x, z, t)$ with respect to its first two variables, viz.

$$\phi_S(a, t) = \sum_{n=0}^{+\infty} \frac{1}{n!}\left[\delta_x \frac{\partial}{\partial x} + \delta_z \frac{\partial}{\partial z}\right]^n \phi_E(x = a', 0, t), \tag{15}$$

with $a' = a + \delta'_x(c = 0, t)$. Further, we expand ϕ_E into a perturbation series

$$\phi_E = \sum_{m=1}^{M} \phi_E^{(m)} + O\left(\varepsilon^{M+1}\right), \tag{16}$$

where $\phi_E^{(m)}$ is a term of order m and M is the truncation order. The chosen small parameter ε is a characteristic oscillatory particle displacement, typically the norm of $\boldsymbol{\delta}$ in (1), divided by a characteristic wavelength. In deep water, the linear amplitudes of δ_x and δ_z are identical, but in shallow water, the amplitude of δ_x becomes larger, typically proportional to $\coth(kh)$ [27], so that the present development is valid for deep water and finite water depth only. By combining (15) and (16), and collecting the terms of same order, we obtain the following triangular system to estimate ϕ_E at $z = 0$:

$$\begin{aligned}
\phi_E^{(1)}(a', 0, t) &= \phi_S(a, t) \\
\phi_E^{(2)}(a', 0, t) &= -\left(\delta_x \frac{\partial \phi_E^{(1)}}{\partial x} + \delta_z \frac{\partial \phi_E^{(1)}}{\partial z}\right) \\
\vdots \quad &= \quad \vdots \\
\phi_E^{(m)}(a', 0, t) &= -\sum_{n=1}^{m-1}\sum_{p=0}^{n} \frac{\delta_x^p \delta_z^{n-p}}{p!(n-p)!} \frac{\partial^n \phi_E^{(m-n)}(a', 0, t)}{\partial x^p \partial z^{n-p}}, \quad \text{for } m > 1.
\end{aligned} \tag{17}$$

Since the horizontal drift δ'_x is the same for all surface particles, a' is the same as the Eulerian x-coordinate within a time-dependent translation. Consequently, the derivatives of $\phi_E^{(m)}$ with respect to x and z in (17) can be computed efficiently from (14) by means of simple Fourier transforms. Finally, the velocity $\nabla\phi_E(x_S, z_S, t)$ of the surface particles can be reconstructed at the order M, viz.

$$\nabla\phi_E(x_S, z_S, t) = \sum_{m=1}^{M}\sum_{n=0}^{m-1}\sum_{p=0}^{n} \frac{\delta_x^p \delta_z^{n-p}}{p!(n-p)!} \frac{\partial^n \nabla\phi_E^{(m-n)}(a', 0, t)}{\partial x^p \partial z^{n-p}} + O\left(\varepsilon^{M+1}\right). \tag{18}$$

The derivation of the surface particle velocity is easily visualized in Fig. 1. The potential ϕ_E known at the blue circles, is first computed on a Eulerian grid at $z = 0$ (red crosses). Then, the Eulerian space derivatives of ϕ_E are calculated at $z = 0$ from (14) to further compute the gradient of ϕ_E back at the particles position with (18).

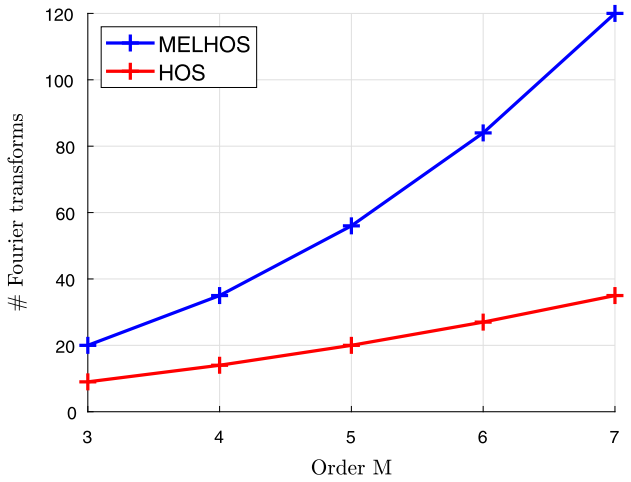

Fig. 2. Number of Fourier transforms per time iteration versus HOS/MELHOS order M.

2.5. Computational cost and comparison with the HOS method

The computational cost of the MELHOS method is directly related to the number of Fourier transforms needed to compute $\nabla\phi_E(x_S, z_S, t)$, which is $(M+3)(M+2)(M+1)/6$. For higher orders M, this is significantly larger than the corresponding value $M(M+3)/2$ for the HOS method [33]. The number of Fourier transforms of the two methods is compared in Fig. 2 for $M = 3 \ldots 7$. The computational burden of the MELHOS method for $M = 3$ and $M = 4$ is then the same as for the HOS-method for $M = 5$ and $M = 7$, respectively. However, as will be shown in the next sections, this is compensated by a faster convergence and by the fact that fewer modes are required to capture steep waves. In practise, HOS-order values of $M = 3$ are generally considered for the simulation of irregular waves [11,34].

2.6. Pressure, acceleration and particle drift

The evolution equations (12) and (13) provide the position and the potential of the surface particles. The velocity inside the whole fluid domain can be reconstructed up to order M from the velocity potential at $z = 0$ from (14) and (17). Following Bernoulli's equation, the Eulerian pressure $p_E(x, z, t)$ reads

$$p_E(x, z, t) = -\rho\left(\dot{\phi}_E + \frac{1}{2}|\nabla\phi_E|^2 + gz\right), \tag{19}$$

where the time derivative $\dot{\phi}_E$ has not been evaluated yet. The mode decomposition (14) used for ϕ_E still applies for its time derivative, viz.

$$\dot{\phi}_E(x, z, t) = \sum_p \dot{A}_p(t)\exp\left(\mathrm{i}k_p x\right)\frac{\cosh\left(k_p[z+h]\right)}{\cosh\left(k_p h\right)}, \tag{20}$$

so that $\dot{\phi}_E$ is also fully determined by its value at $z = 0$. The latter can be obtained by writing that

$$\dot{\phi}_E(x_S, z_S, t) = \dot{\phi}_S(a, t) - |\nabla\phi_E(x_S, z_S, t)|^2 \tag{21}$$

on the surface, and by using the same scheme as for ϕ_E in (17). The acceleration of the surface particles is then

$$\ddot{\boldsymbol{X}}_{\boldsymbol{S}} = -\nabla\left(gz + \frac{p_E}{\rho}\right), \tag{22}$$

where ∇p_E is evaluated at $(x, z) = (x_S, z_S)$ as in (18). By integrating the horizontal acceleration $\ddot{x}_S$, one obtains a horizontal velocity free of any constant drift term. The drift velocity of any particle can then be evaluated as the difference between the term computed in (18) and the one integrated from the horizontal acceleration.

2.7. Numerical implementation

As far as the numerical implementation is concerned, the MELHOS method is rather similar to the standard HOS method. The horizontal and vertical positions x_s and z_s of the surface particles, as well as their velocity potential ϕ_S are computed at a discrete set of N equally-spaced points $a_j = jL/N$ with $j = 0 \ldots N-1$. Here, a_j represents the Lagrangian horizontal

coordinate described in Section 2.1 and j-subscripts in the following refer to the values of a given Lagrangian quantity at $a = a_j$. At $t = 0$, x_{s_j}, z_{s_j} and ϕ_{s_j} are initialized with the Lagrangian linear solution for irregular waves given by e.g. [25]. The smooth transition from the linear to the nonlinear solution is ensured by using the adjustment scheme proposed by [35]. The right-hand sides of the evolution equations (12) and (13) are then split into a linear and a nonlinear part, and the latter is multiplied by a ramp-up function. We use a Runge-Kutta-(4, 5) integrator with adaptive time step to perform the numerical integration, and sensitivity studies showed that a relative tolerance of 10^{-6} was appropriate for the cases presented in this paper. All products of order q were computed by using a full anti-aliasing treatment [5], i.e. by extending the number of Fourier modes to $(q+1)N/2$ with zero-padding. For irregular waves, high-frequency noise was removed with a low-pass filter with a cut-off wave number $k_{cut} = (M+3)k_{max}$, where k_{max} is the wave number of the shortest linear wave component in the spectrum to be simulated. As in the HOS-method, such filtering is beneficial to the stability of the simulations, especially for steep waves [18, p. 28]. First, because super-harmonics of order larger than M, and up to M^2, are generated when estimating the surface velocity with (18), which can be a source of inaccuracies. Then, because possible numerical errors in the highest wavenumber modes get amplified when computing high-order space-derivatives [4]. A possible alternative to low-pass filtering consists in reducing the spatial resolution, which in turn reduces the largest wavenumber, as in [14], who chooses the maximum wavenumber as 5 times the peak wavenumber k_P of the JONSWAP spectrum to be simulated with $M = 3$. For regular wave simulations, the treatment of the high wavenumber modes is described in Section 3.1.3. Finally, due to the periodic boundary conditions, particles drifting out of the domain at $x = L$ will automatically reenter at $x = 0$.

The corresponding Eulerian surface elevation $\eta(x,t)$ can be obtained as a power series truncated at order M, viz.

$$\eta(x,t) = \sum_{m=1}^{M} \eta^{(m)}(x,t) + O\left(\varepsilon^{M+1}\right), \tag{23}$$

where $\eta^{(m)}$ is proportional to ε^m. Since $\eta(a' + \delta_x) = \delta_z$, by using a Taylor expansion, and collecting the terms of same order, we obtain the following triangular system

$$\eta^{(1)}(a',t) = \delta_z(a,t) \tag{24}$$

$$\vdots \quad = \quad \vdots$$

$$\eta^{(m)}(a',t) = -\sum_{n=1}^{m-1} \frac{\delta_x^n}{n!} \frac{\partial^n \eta^{(m-n)}(a',t)}{\partial x^n} \quad \text{for } m > 1. \tag{25}$$

Owing to mass conservation, one should have $\overline{\eta_j} = 0$ and $\overline{z_{s_j}} \neq 0$ from second order [25], where the overline denotes the mean value over the N particles and $\eta_j = \eta(a'_j, t)$. When initializing z_{s_j} with a linear solution, a nonlinear constant term will still be missing in z_{s_j} after the ramp-up phase, which will result in $\overline{\eta_j} < 0$. Consequently, a nonlinear correction equal to $\overline{\eta_j}$ has to be subtracted from z_{s_j} in (13) at each time iteration to ensure that mass conservation is fulfilled up to order M.

3. Verification and convergence tests

3.1. Regular waves

For regular waves, there exist approximated analytical nonlinear solutions for both the Eulerian [31] and the Lagrangian [29,22] flow descriptions. Exact numerical solutions can only be found in the Eulerian formalism [36,37]. In this section, regular waves obtained with the MELHOS method are compared to these solutions in deep water.

3.1.1. Reconstruction of the velocity of the surface particles

First, we show that the proposed numerical scheme is able to propagate the fourth-order Lagrangian solution for a regular wave in deep water. The velocity of the surface particles $(u_S, w_S)^T = \nabla\phi_E(x_S, z_S, t)$ reconstructed with the MELHOS method from the fourth-order expressions of $\boldsymbol{X}_S$ and ϕ_S given by [29] are presented in Appendix A. It is easily seen that $(u_S, w_S)^T$ is equal to the time-derivatives of the particle positions

$$\dot{\mathbf{X}}_\mathbf{S} = \frac{\sigma_0}{k} \begin{bmatrix} \varepsilon^2 + \frac{3}{2}\varepsilon^4 & + & \left(\varepsilon + \varepsilon^3\right)\cos\Psi & + & \frac{2}{3}\varepsilon^4\cos(2\Psi) & + & O\left(\varepsilon^5\right) \\ & & \varepsilon\sin\Psi & + & \frac{1}{3}\varepsilon^4\sin(2\Psi) & + & O\left(\varepsilon^5\right) \end{bmatrix}. \tag{26}$$

Consequently, the evolution equation (12) is fulfilled at order 4 when $\boldsymbol{X}_S$ and ϕ_S are initialized with [29]. Note that (13) is then also fulfilled.

3.1.2. Comparison with Fenton's solution

We now show that the surface elevation η and velocity potential ϕ_E at $z=0$ reconstructed with the MELHOS method are also equivalent to Fenton's Eulerian solution [31] up to the fourth order. From Appendix A, we have

$$k\eta(x,t) = \left[\varepsilon + \frac{\varepsilon^3}{8}\right]\cos\Psi_E + \left[\frac{\varepsilon^2}{2} + \frac{5\varepsilon^4}{6}\right]\cos(2\Psi_E) + \frac{3\varepsilon^3}{8}\cos(3\Psi_E) + \frac{\varepsilon^4}{3}\cos(4\Psi_E) + O\left(\varepsilon^5\right) \tag{27}$$

$$\frac{k^2}{\sigma_0}\phi_E(x,0,t) = \varepsilon\sin\Psi_E + \frac{1}{2}\varepsilon^4\sin(2\Psi_E) + O\left(\varepsilon^5\right) \tag{28}$$

Here, the horizontal drift velocity $\dot{\delta'}_x$ of the surface particles is incorporated into the Eulerian phase $\Psi_E = kx - \sigma_E t$ by writing that

$$\begin{aligned}\sigma_E &= \sigma(0) + k\dot{\delta'}_x(0,t)\\ &= \sigma_0\left(1 + \frac{\varepsilon^2}{2}\right) + O\left(\varepsilon^4\right).\end{aligned} \tag{29}$$

where $\sigma_0^2 = kg$ and $\sigma(c)$ is the depth-dependent Lagrangian wave frequency defined in Appendix A. Equation (29) is recognized as the depth-independent Eulerian wave frequency. The surface elevation and velocity potential given in (27) and (28) are then the same as the expression given in [31], viz.

$$k\eta(x,t) = \left[\varepsilon_E - \frac{3\varepsilon_E^3}{8}\right]\cos\Psi_E + \left[\frac{\varepsilon_E^2}{2} + \frac{\varepsilon_E^4}{3}\right]\cos(2\Psi_E) + \frac{3\varepsilon_E^3}{8}\cos(3\Psi_E) + \frac{\varepsilon_E^4}{3}\cos(4\Psi_E) + O\left(\varepsilon_E^5\right) \tag{30}$$

$$\frac{k^2}{\sigma_0}\phi_E(x,0,t) = \left[\varepsilon_E - \frac{\varepsilon_E^3}{2}\right]\sin\Psi_E + \frac{1}{2}\varepsilon_E^4\sin(2\Psi_E) + O\left(\varepsilon_E^5\right) \tag{31}$$

by writing that

$$\varepsilon = \varepsilon_E\left(1 - \frac{\varepsilon_E^2}{2}\right) + O\left(\varepsilon_E^5\right). \tag{32}$$

Here, ε_E is the small parameter of the Eulerian expansion used in [31], equal to the wave number k times the amplitude of the linear surface elevation, whereas ε is the small parameter of the Lagrangian expansion used in [29].

3.1.3. Numerical simulations of nonlinear regular waves

Further, we initialize x_{s_j}, z_{s_j} and ϕ_{s_j} with a linear solution and perform a time integration over 1000 wave periods with $M=8$, as described in Section 2.7. The fundamental wave number is chosen as $k_0 = \Delta k$, with $\Delta k = 2\pi/L$, and the number of points is $N=32$. All modes with wave numbers $n\Delta k$ and $n > M-2$, corresponding to terms with a leading order $n+2 > M$, were set to zero during the MELHOS simulation. Two simulations are performed with two different amplitudes ε_0/k_0 for the initial linear wave, corresponding to $\varepsilon_0 = 0.100$ and $\varepsilon_0 = 0.355$. The amplitudes of the first five modes of δ_x and δ_z are plotted versus time in Fig. 3 for $\varepsilon_0 = 0.100$, and the amplitudes of the first six modes in Fig. 4 for $\varepsilon_0 = 0.355$. Here, mode 1 refers to the fundamental with wave number k_0, and mode n to super-harmonics with wave number nk_0. After the ramp-up time of 20 linear wave periods $T_0 = 2\pi/\sqrt{k_0 g}$, the obtained nonlinear solutions remain stable during the whole simulation. The new nonlinear wave amplitudes ε/k_0 were estimated from the first two modes by least-square fitting the corresponding amplitudes of the fourth-order solution given in Appendix A. The obtained ε-values are indicated in the title of the figures and they are very close to the initial values ε_0.

The amplitudes of the first five modes of δ_x and δ_z derived from the analytical solution and the fitted ε-values are shown as horizontal black lines. Here, the fourth-order solution given in Appendix A is used for modes $1-2$, and the leading order terms from the seventh-order solution by [22] are used for modes $3-5$. Note that the leading order terms in these two Lagrangian solutions are identical for modes 1 and 2. The match with the amplitudes computed by the MELHOS method is very good for $\varepsilon_0 = 0.100$ in Fig. 3, although some slight differences can be seen for mode 5. For $\varepsilon_0 = 0.355$, however, large discrepancies are found between the analytical solution and the MELHOS amplitudes already from mode 2. These are caused by the presence of terms of order higher than M in the lower modes of the MELHOS solution, whereas these are simply truncated in the analytical solution. Assuming that the highest order terms in x_S, z_S and ϕ_S are proportional to ε^M, it is seen from (18) that the highest order term in $\nabla\phi_E$ is then proportional to ε^{M^2}. Terms with order higher than M are found in the high-frequency modes, and these are generally removed by anti-aliasing and low-pass filtering, but also in the low-frequency ones. For example, the amplitude of the first mode of z_S is $\varepsilon + 1/2\varepsilon^3$ in the fourth-order analytical solution, whereas the amplitude of the same mode computed by the MELHOS method with $M=8$ contains additional higher order terms proportional to $\varepsilon^5, \varepsilon^7, \ldots$. Both solutions are correct up to the fourth order anyhow. For weakly nonlinear waves, the sum of the higher order terms remains small, but for steeper waves like in Fig. 4, it becomes significant. This feature

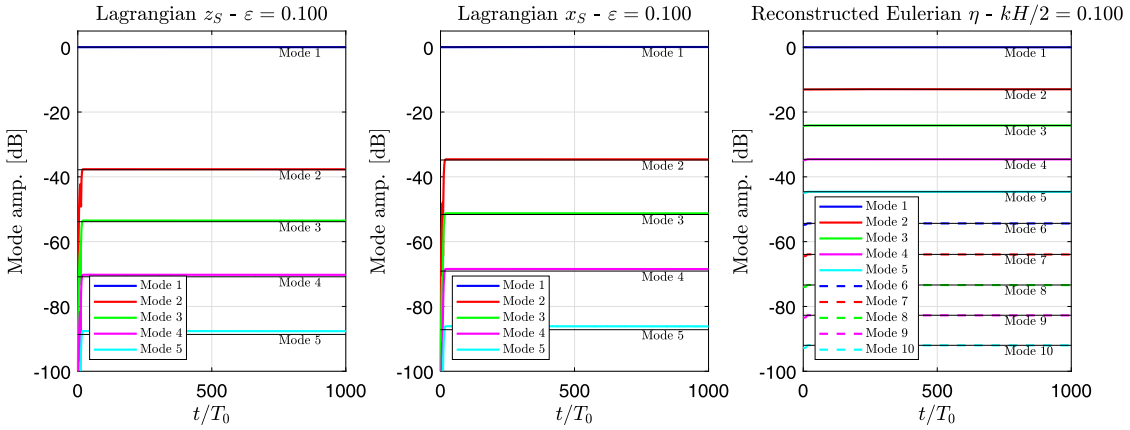

Fig. 3. Relative amplitudes of the first modes of the Lagrangian particle displacement (left and center) and reconstructed Eulerian surface elevation (right) computed with the MELHOS method. Wave steepness $kH/2 = 0.100$ and $M = 8$. Horizontal black lines show the seventh-order Lagrangian solution [22] (left and center), and the exact Eulerian solution [37] (right).

is shared with the HOS method, for which the amplitude of the first mode of η is $\varepsilon - 3/8\varepsilon^3 - 211/192\varepsilon^5$ up to order 5 according to [31].

Next, the Eulerian surface elevation $\eta(x)$ is reconstructed from the position of the surface particles $x_S(a)$ and $z_S(a)$. The Lagrangian spatial resolution is first increased by extending the number of points to $N_{ext} = 2^{13}$ with zero-padding. Then, cubic interpolation is used to compute $\eta(x_j)$ on a regular Eulerian grid x_j with N_{ext} points spanning one wave length. The wave height H can be directly computed from z_S to estimate the Eulerian steepness $\varepsilon_E = k_0 H/2$. The achieved values are $\varepsilon_E = 0.100$ and $\varepsilon_E = 0.380$ for $\varepsilon_0 = 0.100$ and $\varepsilon_0 = 0.355$, respectively. The amplitudes of the first modes of the reconstructed Eulerian surface elevation are plotted in the right hand side of Fig. 3 and Fig. 4. They are compared to the exact solution by [37] computed from the estimated ε_E-values and the same number of points N_{ext}. In both cases, the amplitudes of the Lagrangian harmonics are much smaller compared to their Eulerian counterparts. For example, for the steep wave case with $k_0 H/2 = 0.38$, the relative amplitude of the sixth mode is about -49dB for z_S and -21dB for η. As noticed by [22], the convergence of the Lagrangian solution also appears to be faster. The good match between the reconstructed η and the exact solution shows that the MELHOS method is able to capture the shape of steep regular waves with fewer harmonics, here 6 modes for $M = 8$, compared to an Eulerian approach.

3.1.4. Comparison with the HOS-method and convergence for steep regular waves

In the she standard HOS method introduced by [4,5], the Eulerian surface elevation $\eta(x,t)$ and the velocity potential at the surface $\phi_\Sigma(x,t)$, defined in Section 2.3, are computed by integrating the following system of partial differential equations

$$\dot{\eta} = \left[1 + \left(\frac{\partial \eta}{\partial x}\right)^2\right] W - \frac{\partial \phi_\Sigma}{\partial x}\frac{\partial \eta}{\partial x} \tag{33}$$

$$\dot{\phi}_\Sigma = -g\eta - \frac{1}{2}\left(\frac{\partial \phi_\Sigma}{\partial x}\right)^2 + \frac{1}{2}\left[1 + \left(\frac{\partial \eta}{\partial x}\right)^2\right] W^2, \tag{34}$$

where $W(x,t) = \partial\phi_E/\partial z$ is the vertical particle velocity at the surface $z = \eta(x,t)$, estimated from a truncated series as in (18). The convergence of the HOS-method for steep regular waves has been documented by e.g. [4] and [34]. In these studies, the surface elevation η and the surface potential ϕ_Σ were initialized with the exact solution by [36]. The vertical velocity W was then computed with the HOS-method and compared to the same exact solution. An exponential convergence with respect to the HOS-order M was established for wave steepness values up to $\varepsilon_E = 0.40$. The influence of the number of modes on the convergence was also documented.

An equivalent exact Lagrangian solution, that would describe the particle position x_S and z_S as well as the velocity potential ϕ_S in their vicinity, has not been derived yet to our knowledge. Consequently, it is not possible to compare the convergence of the MELHOS method with the existing results available for the HOS method. Instead, we perform a convergence study by initializing x_S, z_S, ϕ_S, η and ϕ_Σ with linear solutions and by applying a ramp-up function as in [35]. Although this is detrimental to the stability of the numerical scheme for steep waves, it makes it possible to compare the convergence of the HOS and MELHOS methods. In addition, such a linear initialization is more representative of practical simulations of irregular waves. The achieved nonlinear surface elevations and vertical velocities are then compared to the exact solution by [37].

The same numerical set-up as presented in Section 3.1.3 is used for the HOS and MELHOS methods. In particular, all modes with leading order terms ε^{M+1} or less were set equal to zero, namely modes $M-1$ and higher for the MELHOS

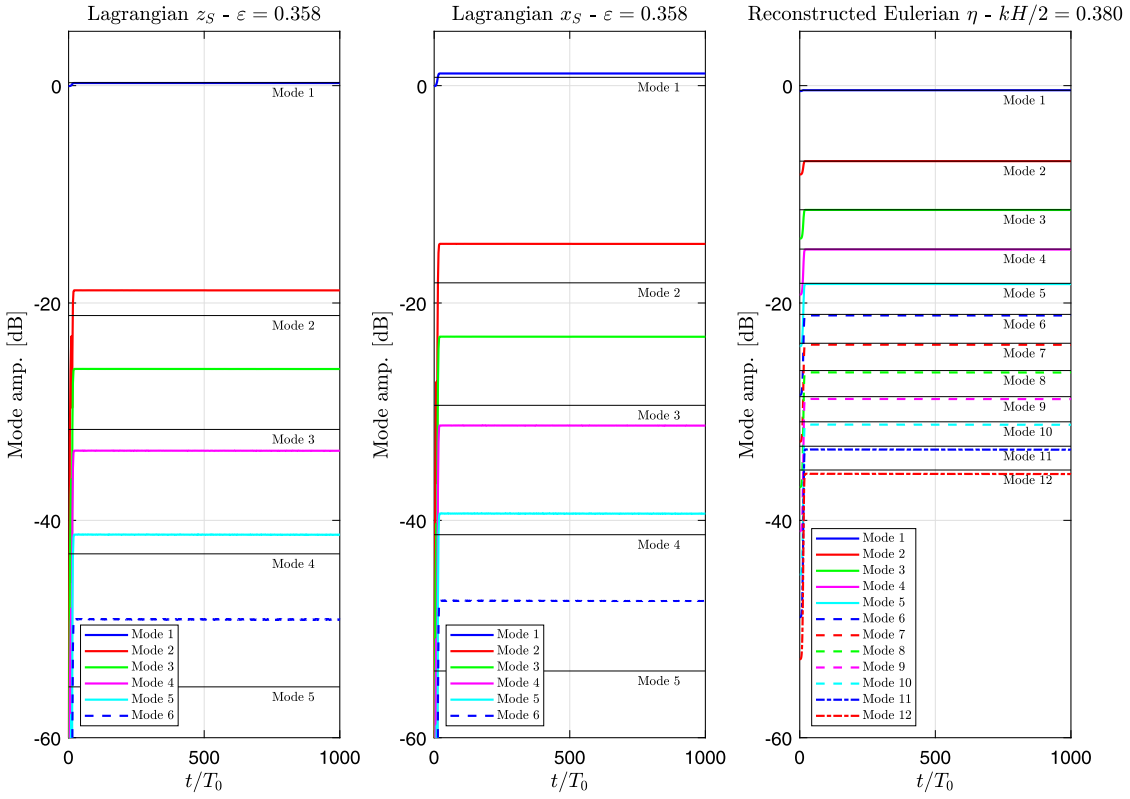

Fig. 4. Relative amplitudes of the first modes of the Lagrangian particle displacement (left and center) and reconstructed Eulerian surface elevation (right) computed with the MELHOS method. Wave steepness $kH/2 = 0.380$ and $M = 8$. Horizontal black lines show the seventh-order Lagrangian solution [22] (left and center), and the exact Eulerian solution [37] (right). The amplitudes of modes 6 for z_S and x_S are of order 8. Eulerian modes with numbers larger than 12 are not displayed.

method, and modes $M+1$ and higher for the HOS method. Such a low-pass filtering improves the stability of the numerical scheme, especially for larger M-values and for the HOS method. Moreover, a full anti-aliasing treatment was applied. The truncation order varies between $M = 3$ and $M = 8$ and the achieved wave steepness is $\epsilon_E = 0.37$ with $M = 8$ for both methods. The relative amplitudes of the first modes obtained with the MELHOS and the HOS methods are plotted for the surface elevation and the velocity potential in Fig. 5. As discussed in the previous section, the MELHOS mode amplitudes are smaller and decrease faster with increasing mode number compared to the standard HOS method.

The relative errors $e_\eta(M)$ and $e_W(M)$, for the surface elevation and the vertical velocity, respectively, are defined as

$$e_\eta(M) = \frac{\max\limits_{x\in[0;2\pi/k_0]} \left|\eta^{(M)}(x) - \eta_C(x)\right|}{\max\limits_{x\in[0;2\pi/k_0]} |\eta_C(x)|} \qquad \text{and} \qquad e_W(M) = \frac{\max\limits_{x\in[0;2\pi/k_0]} \left|W^{(M)}(x) - W_C(x)\right|}{\max\limits_{x\in[0;2\pi/k_0]} |W_C(x)|}, \tag{35}$$

where $\eta_C(x)$ and $W_C(x)$ are the exact surface elevation and vertical velocity by [37], and $\eta^{(M)}(x)$ and $W^{(M)}(x)$ are their counterparts computed at order M from either the MELHOS or the HOS method. The relative errors are plotted in Fig. 6 and show an exponential convergence, as mentioned by [4] and [34]. For the vertical velocity W computed with MELHOS, the convergence is faster for $M = 3-5$, which indicates a weakly nonlinear behaviour as also seen in (26). Overall, the relative errors are smaller with the MELHOS method. For example, with $M = 3$, the Lagrangian solution consists of the fundamental only (mode 1). However, the relative errors e_η and e_W are about the same as for the HOS method with $M = 5$ and $M = 7$, which includes five and seven modes, respectively. The respective computational costs can be found in Fig. 2, which shows that HOS with $M = 5$ is as expensive as MELHOS with $M = 3$, whereas HOS with $M = 7$ is 75% more expensive.

3.2. Bichromatic waves

In this section, we show that the solution obtained with the MELHOS method fulfills the nonlinear Lagrangian conservation equations (3) and (5), up to the selected order M, for a bichromatic wave in deep water. Now, (x_{s_j}, z_{s_j}) and ϕ_{s_j} are initialized with a linear solution that consists of the sum of two regular components with wave numbers k_p and amplitudes ε_p/k_p, for $p = 1\ldots2$. We choose $k_1 = 20\Delta k$, $k_2 = 25\Delta k$, and $\varepsilon_1 = \varepsilon_2 = 0.05$. The corresponding wave periods are denoted

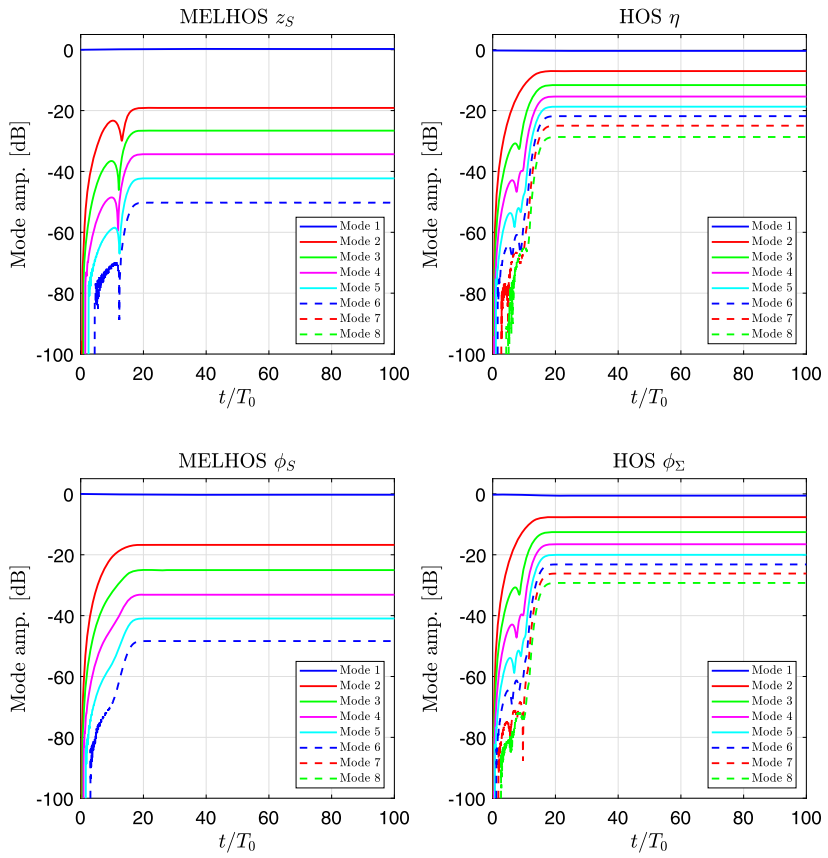

Fig. 5. Comparison of the MELHOS and HOS methods for a steep regular wave with $kH/2 = 0.37$ and $M = 8$.

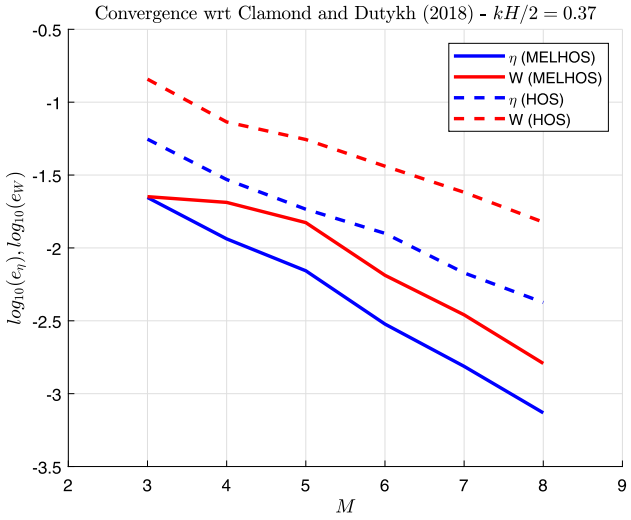

Fig. 6. Convergence of the MELHOS and HOS methods for a steep regular wave with $kH/2 = 0.37$.

$T_p = 2\pi/\sigma_{0p}$ with $\sigma_{0p}^2 = k_p g$. The time integration is performed during 300 wave periods T_1 and the resulting Eulerian surface elevation at the center of the domain is shown in Fig. 7 for $M = 6$. The normalizing parameters k_m and σ_m are chosen as the mean values of k_p and σ_p, respectively, and $T_m = 2\pi/\sigma_m$. The ramp-up duration $30T_m$ is slightly larger than for regular waves to account for difference frequency terms. For $t > 30T_m$, the amplitude of the wave groups is slowly modulated as the result of nonlinear wave-wave interactions, as described by e.g. [9]. The horizontal drift velocity $\dot{\delta}'_x(a, 0, t)$ of the surface particles is derived with the procedure described in Section 2.6, and presented in Fig. 7. Once the nonlinear

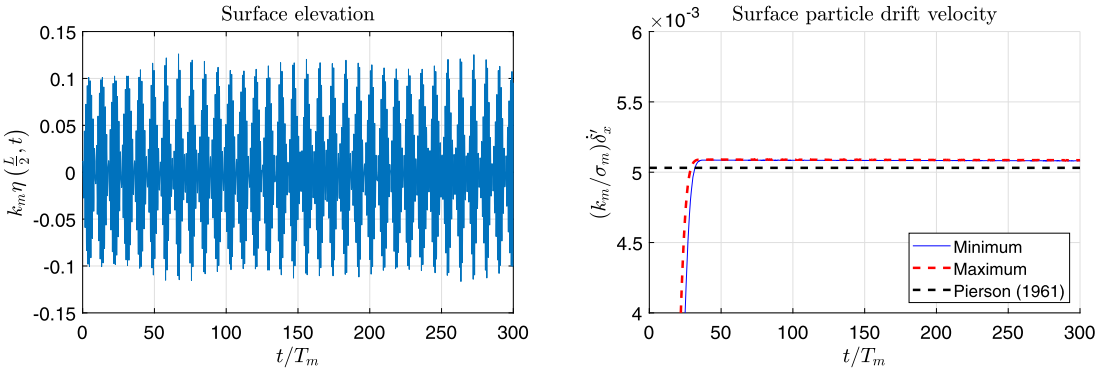

Fig. 7. Eulerian surface elevation at $x = L/2$ (left) and surface particle drift velocity (right) for $M = 6$. The maximum and minimum values are computed from all particles.

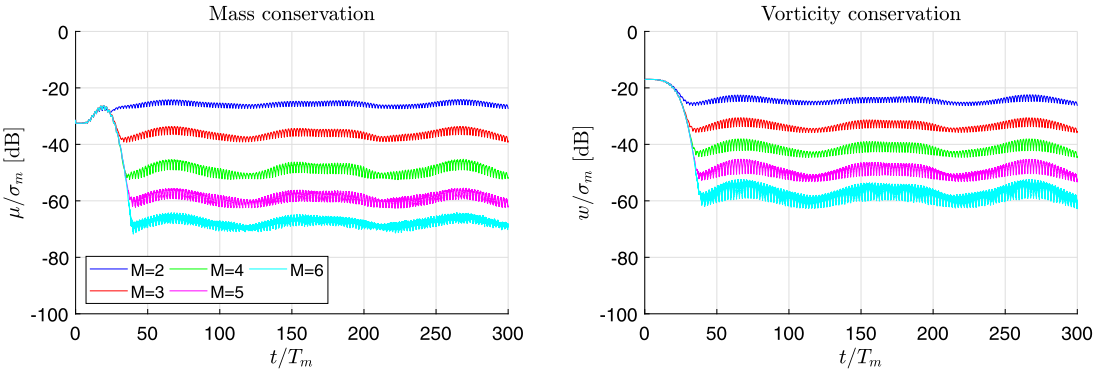

Fig. 8. Residuals of the Lagrangian mass conservation (left) and vorticity (right) at the free surface for a bichromatic wave with $\varepsilon_1 = \varepsilon_2 = 0.05$.

solution has fully developed, all the particles drift at the same constant speed, slightly larger than the second-order value obtained by [25] due to higher-order terms.

The convergence of the solution obtained with the MELHOS method as the order M increases can be assessed by monitoring the two time series

$$\mu(t) = \max_a \left| \frac{\partial\left[\det\left(\boldsymbol{J}\right)\right]}{\partial t} \right| , \qquad w(t) = \max_a \left| \nabla_{\boldsymbol{L}} \times \boldsymbol{J}\dot{\boldsymbol{X}} \right| , \qquad \text{for } c = 0, \tag{36}$$

where $\boldsymbol{J}$ was defined in Section 2.2. The conditions $\mu = 0$ and $w = 0$ correspond to the Lagrangian conservation of mass and zero-vorticity condition, respectively. Here, the partial derivatives with respect to the Lagrangian coordinates a and c are computed numerically by tracking $8N$ additional particles and by using a fourth-order finite difference scheme. The velocities of these particles are derived at each time step from ϕ_E and (14). The convergence of μ and w is shown in Fig. 8 for $M = 2 \ldots 6$. As expected, the convergence speed is about 10dB per order, since $\varepsilon_1 + \varepsilon_2 = 0.1$. It can also be seen that the residuals are stable in time, without secular behaviour, despite some slow variations related to the wave group modulations.

Finally, Fig. 9 shows the time evolution of the modal amplitudes $\hat{x}_s$ and $\hat{z}_s$ of the displacement of the surface particles. Here, $\hat{x}_s$ and $\hat{z}_s$ are computed at each time step as the Fourier transforms of δ_x and δ_z with respect to the Lagrangian coordinate a. The Figure also presents the modal amplitudes $\hat{\eta}$ of the Eulerian surface elevation reconstructed with (27). The two linear modes appear as two red lines, whereas the other horizontal lines correspond to modes resulting from nonlinear interactions. As already noticed for the regular wave case, the number of higher modes needed to capture the surface elevation with the Lagrangian description is much less compared to its Eulerian counterpart.

4. Velocity field in steep waves and comparison with the standard HOS method

The last section of the paper focuses on the simulation of steep irregular waves obtained by nonlinear group focusing, as well as comparisons with the standard HOS-method. The same bichromatic wave as in Section 3.2 is simulated with the MELHOS method, but the amplitudes are increased so that $\varepsilon_1 = \varepsilon_2 = 0.09$. The larger steepness results in a stronger nonlinear modulation of the wave groups and increased energy focusing, as seen in Fig. 10. The same simulation is then performed with the standard HOS method by solving the system of partial differential equation (33)-(34). The same numerical treatment as for the MELHOS method is applied, including domain size, HOS-order M, anti-aliasing and low-pass

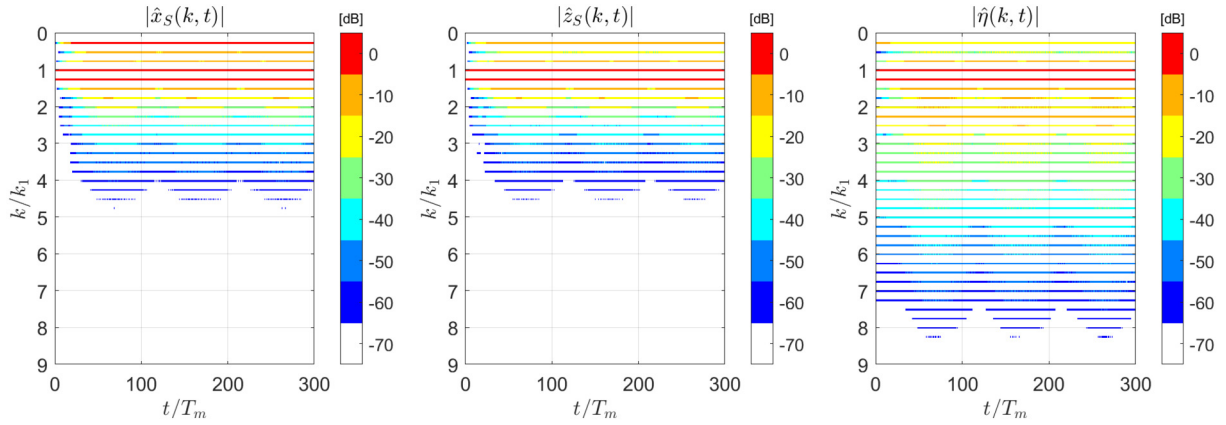

Fig. 9. Modal amplitudes of the horizontal (left) and vertical (center) displacement of the surface particles for $M = 6$, and of the corresponding Eulerian surface elevation (right). All amplitudes are normalized by their value for $k = k_1$ at $t = 0$.

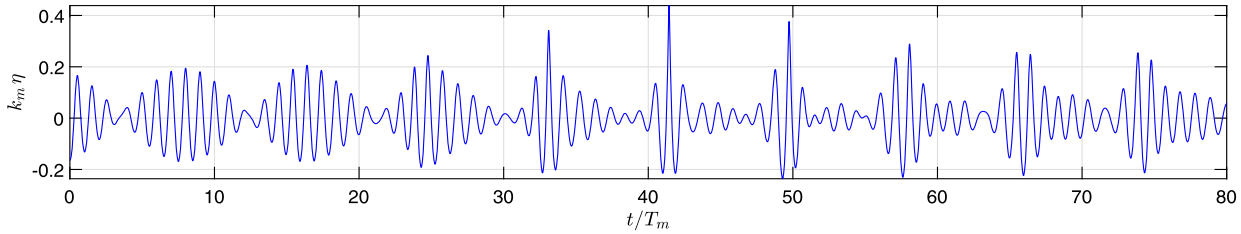

Fig. 10. Time series of the Eulerian surface elevation η computed with the MELHOS method at $k_m x = 110$ with $\varepsilon_1 = \varepsilon_2 = 0.09$ and $M = 4$.

filtering. The spatial discretizations used in both methods, viz. the a_j- and x_j-grids, are the same. In the linear solution used to initialize the simulation, the Eulerian amplitudes are scaled up with (32). This second-order correction is simply based on the fourth-order regular wave solutions by [31] and [29], and we did not perform any optimization of the initial linear amplitudes to ensure that the amplitudes of the nonlinear modes match in both methods. A comparison of the surface elevations obtained with the two methods at the focusing location and time is shown in Fig. 11. The phases of the focused wave are almost identical in the two simulations, although the latter depends on both particle drift and nonlinear phase velocity in the MELHOS method. Far away from the large wave crest, the surface elevations computed by the two methods are also very close. However, the height of the largest crest is about $20 - 25\%$ larger in the MELHOS-simulation. It appears also steeper and sharper due to the horizontal clustering of the fluid particles.

Another major difference between the MELHOS and the HOS method is related to the reconstruction of the velocity field $\nabla\phi_E$ under large wave crests. From (14), it can be seen that the whole velocity field can be derived from $\phi_E(x, z = 0, t)$. With the MELHOS method, the latter can be approximated from the Lagrangian surface variables x_S, z_S and ϕ_S by the Taylor expansion given in (17). The same procedure can be applied with the HOS method to obtain $\phi_E(x, z = 0, t)$ directly from the Eulerian surface variables η and ϕ_Σ, which is often referred to as the H_1-operator [18]. However, [17] showed that this operator may diverge in the vicinity of steep wave crests. Errors made in the nonlinear approximation of $\phi_E(x, 0, t)$ are actually amplified close to the surface due the exponential function in (14). This convergence issue can be circumvented by introducing an iterative procedure, the so-called H_2-operator, which makes it possible to compute the wave kinematics in steep wave crests [17,18,34]. In the present example, the direct computation of the velocity field with the HOS method and the H_1-operator did not converge around the wave crest, as shown in Fig. 12. The equivalent and direct reconstruction of the velocity field from ϕ_S and $\mathbf{X_S}$ with the MELHOS method, however, does not seem to show such limitations. This may be explained by the fact that ϕ_S and $\mathbf{X_S}$ are less nonlinear compared to η and ϕ_Σ, and give therefore better approximations of the flow for steep wave events. The horizontal fluid velocity $u(x, z, t)$ obtained from the same area and time steps as in Fig. 11 is shown in Fig. 13 as an example.

5. Conclusions and further work

In this paper, we have presented a mixed Eulerian-Lagrangian HOS method to simulate the propagation of two-dimensional water waves in constant water depth. We showed that for regular waves in deep water, the numerical simulations are consistent with existing analytical solutions. In addition, the convergence towards an exact solution is demonstrated for a steep regular wave and compared to the standard HOS method. For a weakly nonlinear bichromatic wave, the residuals of the Lagrangian mass conservation and zero-vorticity condition converge towards zero as the trun-

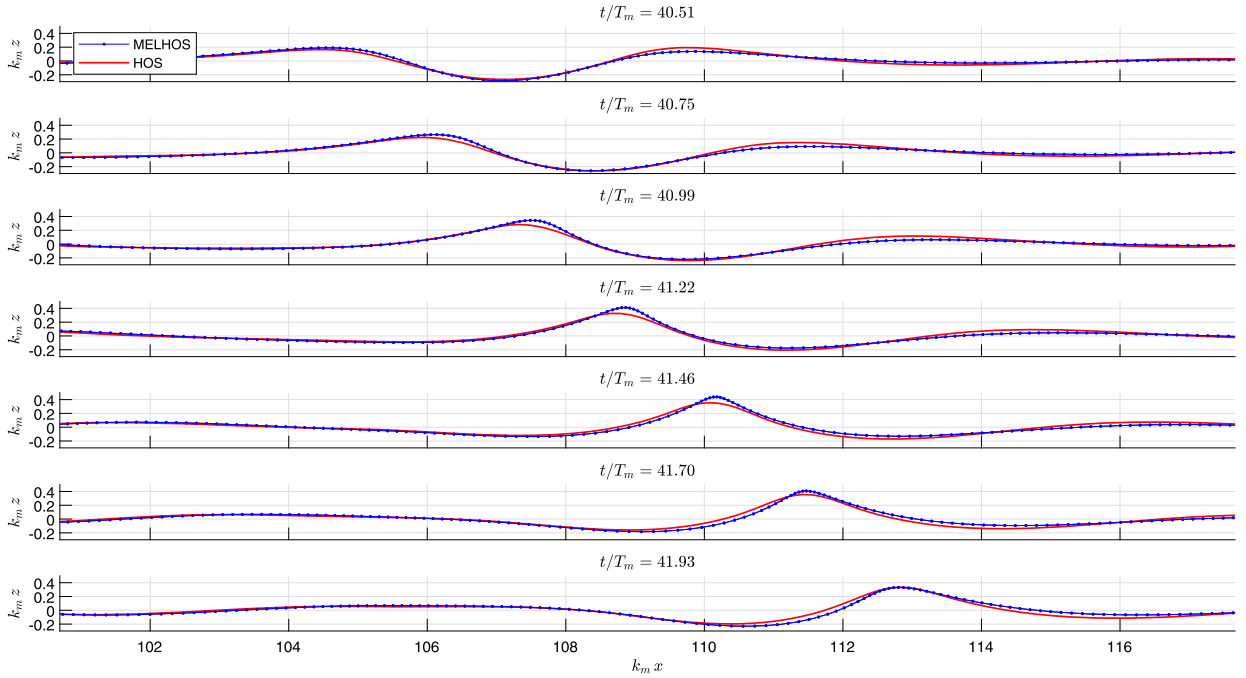

Fig. 11. Comparison of the fourth-order surface elevations obtained from MELHOS and HOS for a steep wave event. Blue dots show the position of the surface particles.

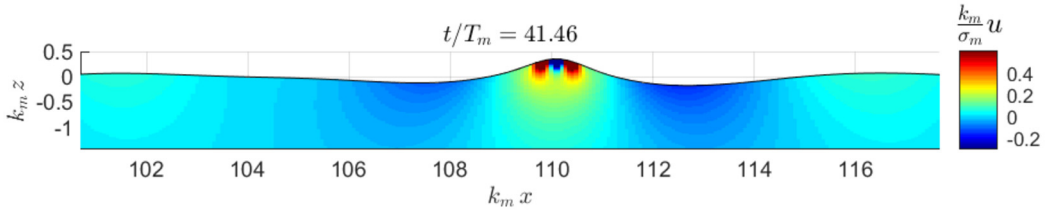

Fig. 12. Fourth-order horizontal fluid velocity $u(x, z, t)$ obtained with the HOS method and the H_1-operator.

cation order M increases from 2 to 6. For both regular and bichromatic waves, the number of modes that are required to capture the free surface with the MELHOS method is significantly reduced compared to the equivalent Eulerian representation. The reconstruction of the velocity field in large and steep wave crests appears more robust with the MELHOS method compared to the standard HOS approach, which requires an additional iterative technique to improve convergence. This characteristic may be related to the fact that, for regular waves in deep water, the velocity potential is more linear when following surface particles than when following the free surface at a constant x-position. Compared to the HOS method, a trade-off is the increased computational cost, which is however no practical limitation for typical truncation orders $M = 3 \ldots 5$.

Nevertheless, the improved numerical stability of the MELHOS simulations for steep irregular waves should be investigated further for longer simulations with realistic wave spectra. Since wave breaking is likely to occur in such sea states, and because it would finally make the MELHOS simulation crash, a numerical damping mechanism to prevent wave overturning should be implemented. An analogous mechanism, based on the ratio of the local energy flux velocity to the local crest velocity, has recently been implemented by [12,13] in the HOS-NWT code [6]. With the Lagrangian representation used in the MELHOS method, the detection of wave breaking can easily be implemented by considering the horizontal distance between two adjacent particles. The extension of the MELHOS method to three-dimensional waves is, in principle, the same as for the HOS approach. However, the existence of a non-homogeneous drift current, which is caused by nonlinear interactions between wave components with the same frequency but different propagation directions [28], raises some challenges. A possible solution would consist in evaluating the two-dimensional drift of each particle with the method described in Section 2.6. Finally, limitations in finite water depth should be investigated, since the horizontal particle displacement tends to increase in shallower water.

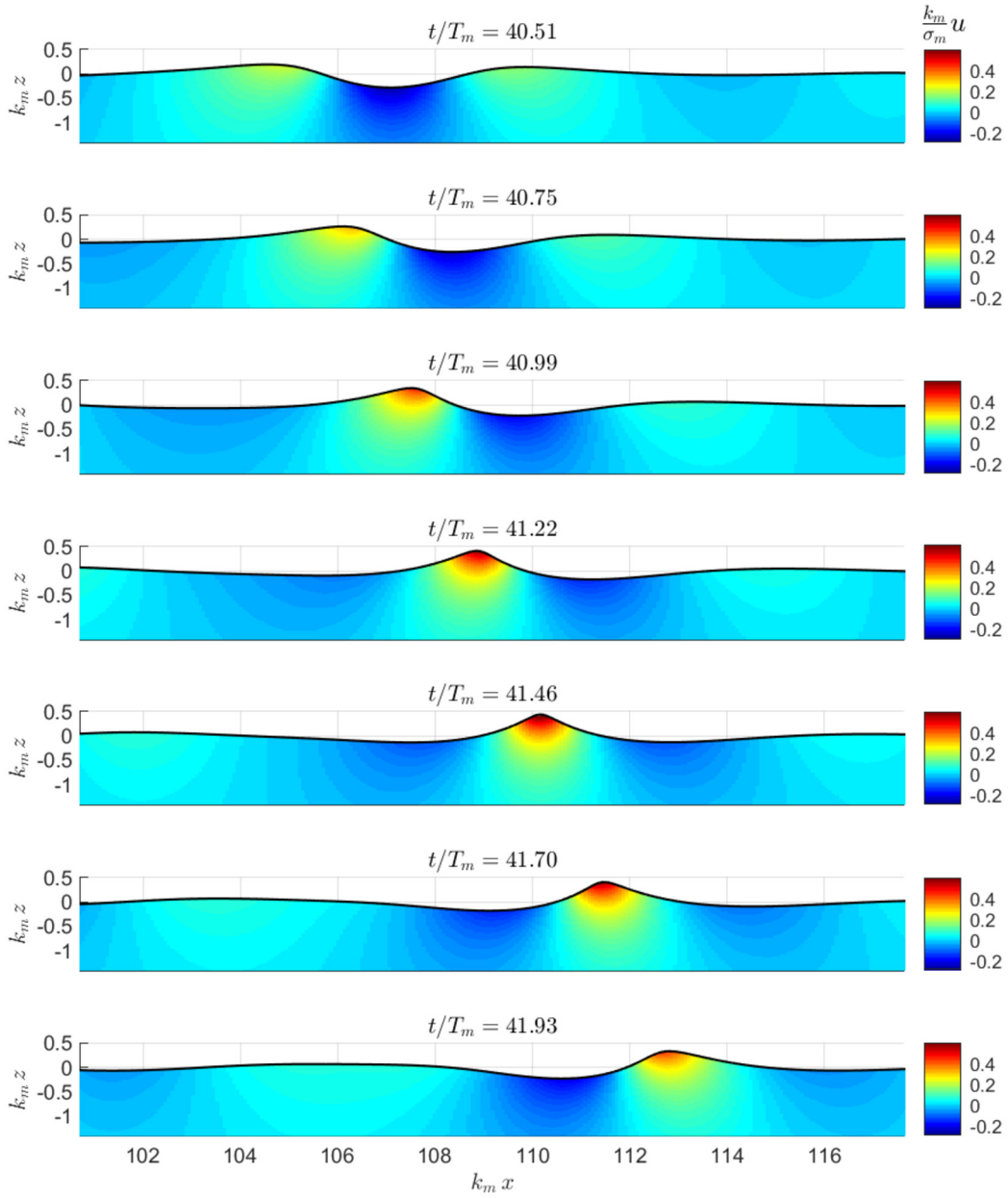

Fig. 13. Fourth-order horizontal fluid velocity $u(x, z, t)$ obtained with the MELHOS method.

CRediT authorship contribution statement

Sebastien Fouques: Conceptualization, Methodology, Software, Investigation, Writing. **Csaba Pakozdi:** Conceptualization, Resources, Validation.

Declaration of competing interest

The authors declare that they have no known competing financial interests or personal relationships that could have appeared to influence the work reported in this paper.

Acknowledgements

The authors are grateful to the Research Council of Norway for the grants provided under the FORINFRA Program (Large Scale Infrastructures), Phase II and III, grants 245956 and 269870, as well as to Erik P. Sande and Silas J. B. Spence for their assistance, and to the reviewers for their constructive comments.

Appendix A. Fourth-order Lagrangian solution for a regular wave in deep water

Following [29], and with the notations of Section 2, the fourth-order Lagrangian solution for a regular wave in deep water can be written as

$$\begin{aligned}
k\delta_x(a,c,t) &= \left[-\varepsilon e^{kc} + \varepsilon^3/2\left(-4e^{3kc} + e^{kc}\right)\right]\sin\Psi + \varepsilon^4/6\left(e^{4kc} - 3e^{2kc}\right)\sin 2\Psi + O\left(\varepsilon^5\right)\\
k\delta_z(a,c,t) &= \left[\varepsilon e^{kc} + \varepsilon^3/2\left(2e^{3kc} - e^{kc}\right)\right]\cos\Psi + \varepsilon^4/6\left(-2e^{4kc} + 3e^{2kc}\right)\cos 2\Psi\\
&\quad + \varepsilon^2/2e^{2kc} + \varepsilon^4/2\left(3e^{4kc} - e^{2kc}\right) + O\left(\varepsilon^5\right)\\
k\delta_x'(c,t) &= \left[\varepsilon^2 e^{2kc} + \varepsilon^4/2\left(4e^{4kc} - e^{2kc}\right)\right]\sigma_0 t + O\left(\varepsilon^5\right)\\
\frac{k^2}{\sigma_0}\phi_L(a,c,t) &= \varepsilon e^{kc}\sin\Psi + \varepsilon^4/6\left(-4e^{4kc} + 3e^{2kc}\right)\sin 2\Psi + O\left(\varepsilon^5\right)
\end{aligned}$$

with $\Psi = ka - \sigma t$, $\sigma(c) = \sigma_0\left[1 + \varepsilon^2/2\left(1 - 2e^{2kc}\right)\right] + O\left(\varepsilon^4\right)$, $\sigma_0^2 = kg$ and $\phi_L(a,c,t) = \phi_E(x_s, z_s, t)$. The Eulerian potential ϕ_E at $z = 0$ and surface elevation η reconstructed with the MELHOS method from the fourth-order Lagrangian solution read

$$\begin{aligned}
\tfrac{k^2}{\sigma_0}\phi_E^{(1)} &= \varepsilon\sin\Psi' - \tfrac{\varepsilon^4}{6}\sin 2\Psi' & k\eta^{(1)} &= \tfrac{\varepsilon^2}{2} + \varepsilon^4 + \left(\varepsilon + \tfrac{\varepsilon^3}{2}\right)\cos\Psi' + \tfrac{\varepsilon^4}{6}\cos 2\Psi'\\
\tfrac{k^2}{\sigma_0}\phi_E^{(2)} &= -\tfrac{1}{2}\varepsilon^3\sin\Psi' + \tfrac{\varepsilon^4}{2}\sin 2\Psi' & k\eta^{(2)} &= -\tfrac{1}{2}\left(\varepsilon^2 + 2\varepsilon^4\right)\left(1 - \cos 2\Psi'\right)\\
\tfrac{k^2}{\sigma_0}\phi_E^{(3)} &= \tfrac{1}{2}\varepsilon^3\sin\Psi' & k\eta^{(3)} &= -\tfrac{3\varepsilon^3}{8}\left(\cos\Psi' - \cos 3\Psi'\right)\\
\tfrac{k^2}{\sigma_0}\phi_E^{(4)} &= \tfrac{\varepsilon^4}{6}\sin 2\Psi' & k\eta^{(4)} &= -\tfrac{\varepsilon^4}{3}\left(\cos 2\Psi' - \cos 4\Psi'\right)
\end{aligned}$$

with $\Psi' = ka' - \sigma t$ and $a' = a + \delta_x'$. The horizontal and vertical velocities of the surface particles, u_S and w_S, respectively, reconstructed with the MELHOS method are then

$$\begin{aligned}
ku_S^{(1)}/\sigma_0 &= \varepsilon\cos\Psi - \tfrac{\varepsilon^4}{3}\cos 2\Psi & kw_S^{(1)}/\sigma_0 &= \varepsilon\sin\Psi - \tfrac{\varepsilon^4}{3}\sin 2\Psi\\
ku_S^{(2)}/\sigma_0 &= \left(\varepsilon^2 + \varepsilon^4\right) + \tfrac{\varepsilon^4}{2}\cos 2\Psi & kw_S^{(2)}/\sigma_0 &= \tfrac{\varepsilon^4}{2}\sin 2\Psi\\
ku_S^{(3)}/\sigma_0 &= \varepsilon^3\cos\Psi & kw_S^{(3)}/\sigma_0 &= 0\\
ku_S^{(4)}/\sigma_0 &= \tfrac{\varepsilon^4}{2} + \tfrac{\varepsilon^4}{2}\cos 2\Psi & kw_S^{(4)}/\sigma_0 &= \tfrac{\varepsilon^4}{6}\sin 2\Psi.
\end{aligned}$$

References

[1] S. Haver, A possible freak wave event measured at the Draupner Jacket, January 1, 1995, in: Proceedings of Rogue Waves 2004, Brest, France, 2004, available at http://www.ifremer.fr/web-com/stw2004/rw/.
[2] T.B. Johannessen, Ø. Hagen, Characteristic levels of strongly nonlinear extreme wave load effects, in: Proceedings of 35th International Conference on Ocean, Offshore and Arctic Engineering, OMAE, ASME, 2016, Paper No. OMAE2016-54963.
[3] M. Perlin, W. Choi, Z. Tian, Breaking waves in deep and intermediate waters, Annu. Rev. Fluid Mech. 45 (2013) 115–145.
[4] D.G. Dommermuth, D.K.P. Yue, A High-Order Spectral method for the study of nonlinear gravity waves, J. Fluid Mech. 184 (1987) 267–288.
[5] B.J. West, K.A. Brueckner, R.S. Janda, D.M. Milder, R.L. Milton, A new numerical method for surface hydrodynamics, J. Geophys. Res. 92 (1987) 11803–11824.
[6] G. Ducrozet, F. Bonnefoy, D.L. Touzé, P. Ferrant, A modified high-order spectral method for wavemaker modeling in a numerical wave tank, Eur. J. Mech. B, Fluids 34 (2012) 19–34.
[7] H. Houtani, T. Waseda, W. Fujimoto, K. Kiyomatsu, K. Tanizawa, Generation of a spatially periodic directional wave field in a rectangular wave basin based on higher-order spectral simulation, Ocean Eng. 169 (2018) 428–441.
[8] V. Zakharov, Stability of periodic waves of finite amplitude on the surfaceof a deep fluid, J. Appl. Mech. Tech. Phys. 9 (1968) 86–94.
[9] M. Onorato, A.R. Osborne, M. Serio, L. Cavaleri, Modulational instability and non-Gaussian statistics in experimental random water-wave trains, Phys. Fluids 17 (2005).
[10] K. Dysthe, K. Trulsen, Note on breather type solutions of the nls as models for freak-waves, Phys. Scr. T 82 (1999) 48–52.
[11] A. Toffoli, O. Gramstad, K. Trulsen, J. Monbaliu, E. Bitner-Gregersen, M. Onorato, Evolution of weakly nonlinear random directional waves: laboratory experiments and numerical simulations, J. Fluid Mech. 664 (2010) 313–336.
[12] B. Seiffert, G. Ducrozet, F. Bonnefoy, Simulation of breaking waves using the high-order spectral method with laboratory experiments: wave-breaking onset, Ocean Model. 119 (2017) 94–104.
[13] B. Seiffert, G. Ducrozet, Simulation of breaking waves using the high-order spectral method with laboratory experiments: wave-breaking energy dissipation, Ocean Dyn. 68 (2018) 65–89.
[14] G. Ducrozet, F. Bonnefoy, Y. Perignon, Applicability and limitations of highly non-linear potential flow solvers in the context of water waves, Ocean Eng. 142 (2017) 233–244.

[15] A. Alberello, C. Pakozdi, F. Nelli, E. Bitner-Gregersen, A. Toffoli, Three dimensional velocity field underneath a breaking rogue wave, in: Proceedings of 36th International Conference on Ocean, Offshore and Arctic Engineering, OMAE, ASME, 2017, Paper No. OMAE2017-61237.
[16] A. Alberello, A. Iafrati, The velocity field underneath a breaking rogue wave: laboratory experiments versus numerical simulations, Fluids 4 (2019) 68.
[17] W.J.D. Bateman, C. Swan, P.H. Taylor, On the calculation of the water particle kinematics arising in a directionally spread wavefield, J. Comput. Phys. 186 (2003) 70–92.
[18] G. Ducrozet, Modélisation des processus non-linéaires de génération et de propagation d'états de mer par une approche spectrale, Technical Report, Ecole Centrale de Nantes, France, 2008, PhD Thesis, HAL Id: tel-00263596 https://tel.archives-ouvertes.fr/tel-00263596.
[19] M.S. Longuet-Higgins, E.D. Cokelet, The deformation of steep surface waves on water. I. A numerical method of computation, Proc. R. Soc. Lond. A 350 (1976) 1–26.
[20] H. Lamb Hydrodynamics, 6 ed., Cambridge University Press, 1932.
[21] E.V. Buldakov, P.H. Taylor, R.E. Taylor, New asymptotic description of nonlinear water waves in Lagrangian coordinates, J. Fluid Mech. 562 (2006) 431–444.
[22] D. Clamond, On the Lagrangian description of steady surface gravity waves, J. Fluid Mech. 589 (2007) 433–454.
[23] F.J. Gerstner, Theorie der wellen, Gilbert's Ann. Phys. XXXII (1809).
[24] D. Henry, On Gerstner's water wave, J. Nonlinear Math. Phys. 15 (2008) 87–95.
[25] W.J. Pierson, Models of random seas based on the Lagrangian equations of motion, Technical Report, Tech. Rept. Contr. Nonr-285(03), College og Engineering, New York University, 1961.
[26] S.H. Gjøsund, A Lagrangian model for irregular waves and wave kinematics, J. Offshore Mech. Arct. 125 (2003) 94–102.
[27] S. Fouques, H.E. Krogstad, D. Myrhaug, A second-order Lagrangian model for irregular ocean waves, J. Offshore Mech. Arct. 128 (2006) 177–183.
[28] F. Nouguier, B. Chapron, C.A. Guérin, Second-order Lagrangian description of tri-dimensional gravity wave interactions, J. Fluid Mech. 772 (2015) 165–196.
[29] Y.Y. Chen, H.S. Chen, Lagrangian solution for irrotational progressive water waves propagating on a uniform current: Part 1. Fifth order analysis, Ocean Eng. 88 (2014) 546–567.
[30] S. Fouques, C.T. Stansberg, A modified linear Lagrangian model for irregular long-crested waves, in: Proceedings of 28th International Conference on Ocean, Offshore and Arctic Engineering, OMAE, ASME, 2009, Paper No. OMAE2009-79752.
[31] J.D. Fenton, A fifth-order Stokes theory for steady waves, J. Waterw. Port C-ASCE 111 (1985) 216–234.
[32] H.-K. Chang, J.-C. Liou, M.-Y. Su, Particle trajectory and mass transport of finite-amplitude waves in water of uniform depth, Eur. J. Mech. B, Fluids 26 (2007) 385–403.
[33] H. Schäffer, Comparison of Dirichlet–Neumann operator expansions for nonlinear surface gravity waves, Coast. Eng. J. 55 (2008) 288–294.
[34] G. Ducrozet, F. Bonnefoy, D.L. Touzé, P. Ferrant HOS-ocean, Open-source solver for nonlinear waves in open ocean based on high-order spectral method, Comput. Phys. Commun. 203 (2016) 245–254.
[35] D.G. Dommermuth, The initialization of nonlinear waves using an adjustment scheme, Wave Motion 32 (2000) 307–317.
[36] M.M. Rienecker, J.D. Fenton, A Fourier approximation method for steady water waves, J. Fluid Mech. 104 (1981) 119–137.
[37] D. Clamond, D. Dutykh, Accurate fast computation of steady two-dimensional surface gravity waves in arbitrary depth, J. Fluid Mech. 844 (2018) 491–518.